Applied Energy 167 (2016) 17–33

Contents lists available at ScienceDirect

Applied Energy

journal homepage: www.elsevier.com/locate/apenergy

The definition of non-dimensional integration temperature difference and its effect on organic Rankine cycle

Xufei Yang, Jinliang Xu *, Zheng Miao, Jinghuang Zou, Fengliang Qi

The Beijing Key Laboratory of Multiphase Flow and Heat Transfer, North China Electric Power University, 102206 Beijing, China

HIGHLIGHTS

- Two non-dimensional integration temperature differences are newly defined.
- Integration temperature differences are experimentally determined.
- The first non-dimensional temperature difference is linear to the specific exergy losses.
- Performance parameters reach maximum at a specific integration temperature difference.
- Integration temperature difference guides engineers to optimize the ORC system.

ARTICLE INFO

Article history:
Received 22 October 2015
Received in revised form 25 December 2015
Accepted 16 January 2016

Keywords:
Organic Rankine cycle
Integration temperature difference
Exergy
Heat transfer

ABSTRACT

The integration temperature difference ΔT_i considers the heat transfer routes, linking the heat transfer process with the thermodynamic behavior of heat exchangers. The first and second non-dimensional integration temperature differences are defined as $\Delta T^*_{i,h} = \Delta T_i/T_{h,i}$ and $\Delta T^*_{i,s} = \Delta T_i/(T_{h,i} - T_0)$ respectively, where $T_{h,i}$ is the heat source temperature and T_0 is the environment temperature. This paper is the first to experimentally verify the significance of the non-dimensional integration temperature differences on organic Rankine cycle (ORC) systems. The first non-dimensional temperature difference is shown to have linear relationship with the revised entropy generation numbers (N_s). With increases of the second non-dimensional integration temperature difference, the expander powers, system thermal and exergy efficiencies had parabola distributions. They simultaneously reached maximum at $\Delta T^*_{i,s} = 0.282$, under which the vapor cavitation in the expander disappears and the exergy losses of heat exchangers are acceptable to elevate the expander efficiency. Beyond the optimal point, the ORC performance is worsened either due to the vapor cavitation in the expander, or due to the poor thermal matches in the evaporator and condenser. The second non-dimensional integration temperature difference comprehensively reflects the effects of heat source temperatures, heating powers and organic fluid flow rates and pressures, etc. It balances exergy destructions of various components to optimize the system. Thus, it can be an important parameter index to maximize the power or electricity output for a specific heat source. The usefulness of the integration temperature difference and the future work are discussed in the end of this paper.

1. Introduction

Organic Rankine cycle (ORC) has been widely investigated. ORC converts low grade thermal energy to mechanical work or electricity. The heat source to drive ORC can be solar thermal energy [1–5], geothermal energy [6–9], biomass energy [10,11] and various waste heat sources such as flue gas [12–18].

A basic ORC consists of a pump, an evaporator, an expander (or a turbine) and a condenser. The performances of these components play important roles on ORC. The system performance is relied on exergy destructions contributed by these components. Usually, the exergy destruction of the pump is small and can be neglected. The evaporator, expander and condenser are strongly coupled with each other. In ORC system, evaporator is the key component to couple the heat carrier fluid of the heat source (such as flue gas or solar energy) with the organic fluid. A better coupling between the heat source and the organic fluid increases the ORC thermal efficiency and/or heat utilization degree of the heat source

* Corresponding author. Tel./fax: +86 010 61772613.
E-mail address: xjl@ncepu.edu.cn (J. Xu).

http://dx.doi.org/10.1016/j.apenergy.2016.01.037

Nomenclature

C_p	specific heat capacity at constant pressure, J/(kg K)
d	diameter, mm
E	exergy, W
ex	specific exergy, J/kg
f	frequency, Hz
h	specific enthalpy, J/kg
I	exergy destruction, W
L	the evaporator tube length, m
m	mass flow rate, kg/h
M	torque, N m
N_s	revised entropy generation number
n	rotating speed, rpm
Q	heat transfer rate, W
P	pressure, Pa
s	specific entropy, J/(kg K)
T	temperature, °C or K
W	work, W
x	one-dimensional coordinate, m
ΔS	entropy, J/K
ΔT_{i}	expander inlet and outlet temperature difference in evaporator, °C, K
ΔT_{exp}	integration temperature difference in evaporator, °C, K
$\Delta T_{\mathrm{log\text{-}m}}$	logarithmic-mean-temperature-difference, °C, K
$\Delta T^*_{\mathrm{i,h}}$	first non-dimensional temperature difference
$\Delta T^*_{\mathrm{i},s}$	second non-dimensional temperature difference
MFM	mass flow meter

Greek symbols

λ	thermal conductivity, J/(kg K)
η_{exp}	expander efficiency
η_{net}	ORC thermal efficiency
η_{ex}	ORC exergy efficiency
η_T	exergy temperature
v	kinematic viscosity, m^2/s
ρ	density, kg/m^3
Φ	diameter, mm

Subscripts

a	available
c	cooling water, cold fluid
cr	critical
con	condensing
e	evaporating
exp	expander
h	hot fluid
i	integration, inlet or ideal
me	measurement
max	maximum
min	minimum
net	net
o	outlet
oil	conductive oil
others	pipes between expander and heat exchangers
pump	pump
r	working fluid (R123 fluid in this study)
s	isentropic, system
sat	saturated
sup	superheated
sub	sub-cooling
t	total
0	reference state
1–5	state points along the ORC cycle
1	expander inlet
2	expander outlet
2′	condenser inlet
3	pump inlet, condenser outlet
4	pump outlet, evaporator inlet
5	evaporator outlet

[17,19]. Due to this reason, the transcritical ORC was proposed to avoid the isothermal evaporation in the evaporator [20,21]. Alternatively, the zeotropic mixture fluid increases the temperatures by heating to improve the coupling between the heat carrier fluid and the organic fluid. ORCs with mixture working fluid are better than those using the pure organic fluid [22,23].

Vapor expansion in the expander needs high quality vapor generated by the evaporator. The classical thermodynamic theory assumes the saturated vapor inlet to maximize the work output [24,25]. The recent experimental study by Yang et al. [26] shows that the saturated vapor inlet causes the vapor cavitation in the expander to decrease the mechanical work. A vapor superheating degree of about 13 °C is necessary to avoid the vapor cavitation. On the other hand, ultra-high vapor superheating degree worsens the system performance. Thus, the mechanical work generated by the expander shows the parabola distribution versus the vapor superheating degrees at the expander inlet. The condenser cools the vapor at the expander outlet to the subcooled liquid. Thus, the liquid can be recycled by the pump. A low pressure in the condenser increases the pressure ratio of the expander to improve the ORC performance. In addition to this, high superheating vapor at the condenser inlet worsens the thermal match between the organic fluid and the cooling media in the condenser.

Song and Gu [27] designed a dual loop ORC system to recover the waste heat of a diesel engine. The high temperature (HT) loop utilizes the waste heat of the engine exhaust gas, and the low temperature (LT) loop uses the heat load of the jacket cooling water and the residual heat of the HT loop sequentially. It was shown that the maximum net power output of the dual loop ORC reaches 115.1 kW, leading to an increase of 11.6% of the original power output of the diesel engine. Maraver et al. [28] studied the thermodynamic optimization of ORCs for power generation and CHP from different heat sources. An optimization model of the ORC system was proposed to predict the best cycle performance (subcritical or transcritical), in terms of the exergy efficiency, with different working fluids. The purely thermodynamic approach is limited by the technological constraints of the expander, the heat exchangers and the feed pump. Hence, a complementary assessment of both approaches is more adequate to obtain some preliminary design guidelines for ORCs. Toffolo et al. [29] pointed out that the cycle configuration, working fluid and operating parameters are crucial for the economic profitability of ORC systems. Several optimization criteria were used at the same time: the thermodynamic optimization, the deign options around the optimum values of the objective function, an economic modeling technique validated on real cost data, and the consideration of the off-design behavior. The fluid R134a had better cycle performance than isobutane. The results highlighted the alternative design conditions to those maximizing the power output which might be preferred for technical and economic reasons. Lee et al. [30] proposed an innovative approach to collect the solar thermal energy from the concept of solar chimneys for electricity generation via ORCs. In a feasibility analysis of ORC application, the system provides the buildings with 12 kW h/day of electricity, and the area of the collector was 41 m^2. The experimental results indicated that the proposed method is feasible for solar chimney, providing acceptable quality and quantity of heat for ORC.

In summary, many factors are coupled with each to influence the ORC performance. The ORC optimization was performed by many researchers [7,15,31–34]. The optimization procedure not only contains many thermal-fluid parameters such as pressures, temperatures and mass flow rates, but also involves some economical parameters such as fabrication and operation costs of the ORC system [33,34].

Here, we explore the evaporator effect on the ORC performance. The evaporator couples ORC with the heat source. Because evaporator operates at the highest temperature level among ORC components, it contributes large percentage of the total exergy destruction of the ORC system. Thus, the evaporator dominates the ORC performance, from the thermodynamics point of view. The problems are how to quantify the evaporator effect on the ORC system? What is the coupling mechanism between heat carrier fluid and organic fluid in the evaporator?

In order to answer above questions, Chen et al. [17] proposed a new design method to couple the ORC with the heat source. The heat source was characterized by the mass flow rate, inlet and outlet temperatures of the heat carrier fluid. The similarity triangle principle was used to make the solution convergence. The method relates the turbine power with the system thermal efficiency and ensures engineers to recover the waste heat with its flue gas exit temperature as low as possible.

Subsequently, Xu and Yu [19] proposed the integration temperature difference of the evaporator ($\triangle T_i$) to quantify the thermal match between the heat carrier fluid of the heat source and the ORC system. The integration temperature difference is the enclosed area of the T–Q curves across the two side fluids divided by the total heat transfer rate, in which T is the temperature and Q is the heat. It is found that $\triangle T_i$ is related to the exergy destruction of the evaporator. The integration temperature difference concept yields the critical temperature criterion for working fluid selection. The ORC thermal efficiency is higher when the critical temperature of the organic fluid approaches the heat source temperature, under which the enclosed area of the T–Q curves is small.

Recently, the integration temperature difference was extended to analyze the transcritical pressure ORC [20]. The organic fluid undergoes a protruded T–Q curve section and a concaved T–Q curve section, interfaced at the pseudo-critical temperature point. The increase of critical temperatures of organic fluids elongates the specific heat increment section and shortens the specific heat decrease section to decrease the enclosed area of the T–Q curves of the heat carrier fluid and the organic fluid. The integration temperature difference concept successfully explains the ORC performance influenced by the critical temperatures of organic fluids.

The available work on the integration temperature difference regards the theoretical analysis. The experimental work on this topic is not reported before. The objective of this paper is to experimentally verify the usefulness of the integration temperature difference. Different from the previous studies [19,20], the new contribution of this paper is as follows:

- Define the first and second non-dimensional integration temperature differences.
- An ORC machine was developed to ensure necessary measurements.
- Totally 52 thermocouples were arranged along the evaporator flow length to experimentally determine the integration temperature difference.
- It is found that the first non-dimensional integration temperature difference is linearly related to the specific exergy destruction of the evaporator.
- It is found that expander mechanical work, net system thermal efficiencies and exergy efficiencies simultaneously reach maximum when the second non-dimensional integration temperature difference equals to 0.282.

2. Definition of two non-dimensional integration temperature differences

We define the integration temperature difference for heat exchangers. Then, we define the first non-dimensional integration temperature difference for the heat exchanger performance, and the second non-dimensional integration temperature difference for the system performance. A counter current heat exchanger is considered with a hot fluid entering the heat exchanger at temperature $T_{h,i}$ and leaving the heat exchanger at temperature $T_{h,o}$. Meanwhile, the cold fluid enters the heat exchanger at temperature $T_{c,i}$ and leaves the heat exchanger at temperature $T_{c,o}$. The total heat transfer rate is Q_t. Fig. 1a shows the T–Q curve, in which the subscripts h and c stand for the hot fluid and cold fluid, respectively, the subscripts i and o means inlet and outlet, respectively. The pinch temperature is recorded as ΔT_p. The integration temperature difference is defined as

$$\Delta T_{\rm i} = \frac{\int_0^{Q_t}(T_{\rm h} - T_{\rm c})dQ}{Q_{\rm t}} \tag{1}$$

The integration temperature difference is so called because it contains the integration term $\int_0^{Q_t}(T_{\rm h} - T_{\rm c})dQ$ in Eq. (1), which is the enclosed area formed by the T–Q curves of hot and cold fluids (see Fig. 1a). The first non-dimensional integration temperature difference $\Delta T^*_{\rm i,h}$ is defined for the heat exchanger as

$$\Delta T^*_{\rm i,h} = \frac{\Delta T_{\rm i}}{T_{\rm h,i}} = \frac{\int_0^{Q_t}(T_{\rm h} - T_{\rm c})dQ}{T_{\rm h,i}Q_{\rm t}} \tag{2}$$

Equation (2) tells us that $\Delta T^*_{\rm i,h}$ is $\Delta T_{\rm i}$ referenced to $T_{\rm h,i}$ at which the hot fluid enters the heat exchanger. $\Delta T^*_{\rm i,h}$ evaluates the heat exchanger performance only. The exergy temperature at temperature T is defined as

$$\eta_T = 1 - \frac{T_0}{T} \tag{3}$$

where T_0 is the reference temperature, which can be the environment temperature. Further, we divide $\Delta T^*_{\rm i,h}$ by the exergy temperature at temperature $T_{\rm h,i}$ to obtain the second non-dimensional integration temperature difference $\Delta T^*_{{\rm i},s}$, which considers the effect of heat exchanger on the thermal-power conversion system. The subscript s means system. $\Delta T^*_{{\rm i},s}$ is

$$\Delta T^*_{{\rm i},s} = \frac{\Delta T^*_{\rm i,h}}{\eta_{T_{\rm h,i}}} = \frac{\Delta T_{\rm i}}{T_{\rm h,i} - T_0} = \frac{\int_0^{Q_t}(T_{\rm h} - T_{\rm c})dQ}{(T_{\rm h,i} - T_0)Q_{\rm t}} \tag{4}$$

Fig. 1b plots η_T versus Q. The exergy destruction I is the enclosed area formed by the curves of the hot fluid and cold fluid, which is

$$I = \int_0^{Q_t}(\eta_{T,\rm h} - \eta_{T,\rm c})dQ = T_0\int_0^{Q_t}\frac{(T_{\rm h} - T_{\rm c})}{T_{\rm h}T_{\rm c}}dQ \tag{5}$$

We divide I by Q_t, and record I/Q_t as the specific exergy destruction. Based on refs. [35,36], for a heat exchanger, the revised entropy generation number (N_s) is defined as

$$N_s = \frac{T_0\Delta S}{Q_{\rm t}} = \frac{I}{Q_{\rm t}} \tag{6}$$

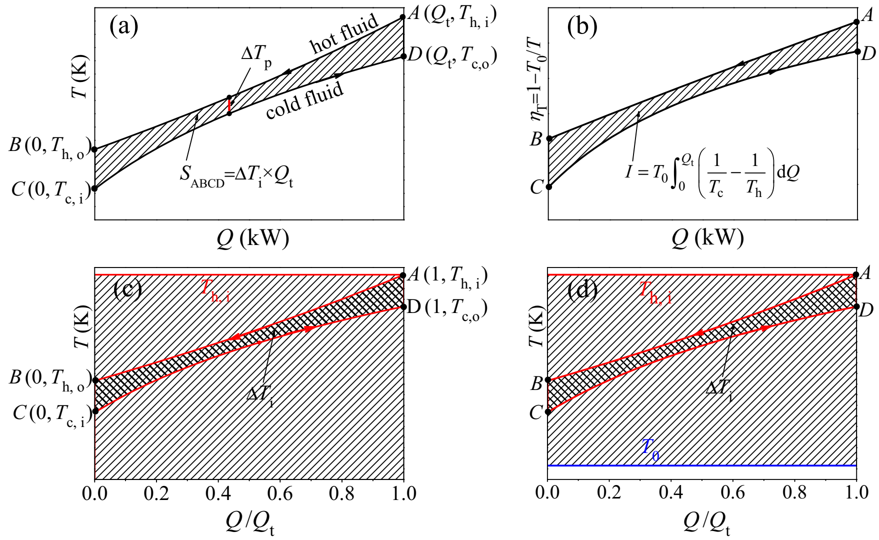

Fig. 1. Definitions of the integration temperature difference and non-dimensional integration temperature difference for heat exchangers (a) *T*–*Q* curve of the hot and cold fluids with the enclosed area representing the integration temperature difference times the total heat transfer rate, (b) the exergy temperature versus heat transfer rates with the enclosed area representing the exergy destruction, (c) the temperatures of hot and cold fluids versus non-dimensional heat transfer rates, the first non-dimensional integration temperature difference is the enclosed area *ABCD* divided by the rectangular area with the temperature range of 0 ~ $T_{h,i}$, and (d) the temperatures of hot and cold fluids versus non-dimensional heat transfer rates, the second non-dimensional integration temperature difference is the enclosed area *ABCD* divided by the rectangular area with the temperature $T_{h,i}$ referenced to the environment temperature T_0.

where ΔS is the entropy increment during the heat transfer process, we see that the revised entropy generation number (N_s) equals to the specific exergy destruction (I/Q_t). Fig. 1a shows the *T*–*Q* curve, in which the enclosed area is $\Delta T_i \times Q_t$. Fig. 1b plots η_T–*Q*, in which the enclosed area is the exergy destruction (*I*). Fig. 1c plots *T*–(Q/Q_t) curve. The non-dimensional heat transfer rate Q/Q_t covers the range of 0–1 and the enclosed area is ΔT_i. The first non-dimensional integration temperature difference $\Delta T^*_{i,h}$ (see Eq. (2)) is the curve enclosed area ΔT_i divided by the rectangular area formed between the two temperatures of $T = T_{h,i}$ and $T = 0$ K. Alternatively, the second non-dimensional temperature difference $\Delta T^*_{i,s}$ is ΔT_i divided by the rectangular area formed by the two temperatures of $T = T_{h,i}$ and $T = T_0$ (see Fig. 1d).

The objective of the present work is to: (1) explore the relationship between $\Delta T^*_{i,h}$ and N_s, (2) explore the effect of $\Delta T^*_{i,s}$ on the ORC system performance, experimentally. As a process parameter, the integration temperature difference reflects the heat transfer route to fully consider the integration effect of the heat transfer process. Thus, it is connected with the irreversible exergy loss in the heat transfer process. Some temperature differences are defined in thermodynamic and heat transfer textbooks. A commonly used one is the logarithmic-mean-temperature-difference [37]:

$$\Delta T_{\log-m} = \frac{\Delta T_{max} - \Delta T_{min}}{\ln \frac{\Delta T_{max}}{\Delta T_{min}}} \tag{7}$$

Referring to Fig. 1a,

$$\Delta T_{max} = \max[(T_{h,i} - T_{c,o}), (T_{h,o} - T_{c,i})],$$
$$\Delta T_{min} = \min[(T_{h,i} - T_{c,o}), (T_{h,o} - T_{c,i})] \tag{8}$$

Eq. (8) is useful for the heat transfer area estimation but it has no connection with the exergy destruction in heat exchangers. For identical logarithmic-mean-temperature-differences, the exergy destructions may be different. The logarithmic-mean-tempera ture-difference is a state parameter. It is determined by two side locations without considering the heat transfer route. Many references used the pinch temperature difference [38–40], which is recorded as $\Delta T_p = \min(T_h - T_c)$ (see Fig. 1a). Because the pinch occurs at a specific location, it definitely cannot reflect the integration effect of the heat transfer process over the whole flow length.

3. The experimental system and method

3.1. The ORC system

Fig. 2a shows the ORC cycle, consisting of four subsystems, represented by four different colors. The four subsystems are coupled with each other. These subsystems are described as follows.

3.1.1. The working fluid loop (black color)

The ORC loop consists of a piston pump, an evaporator, an expander and a condenser. The piston pump circulates the R123 fluid. A frequency converter was connected with the pump to change the pumping flow rate. The fluid R123 has a critical temperature of 184 °C, which is suitable for the heat source temperature below 200 °C, based on the critical temperature criterion for working fluid selection (see Xu and Yu [19]). The evaporator is a concentric tube heat exchanger, with R123 fluid flowing inside the inner tube and conductive oil flowing in the tube annulus. Later we will give the detailed description of the heat exchanger. The expander is modified from a scroll compressor, which is a commercial product used in air-conditioning system installed in bus. It is considered as one of the promising candidates for the expander in ~kW scale [26,41]. The mechanical work of the expander is about 4 kW. Some modifications are performed so that it is suitable to work as an expander: (1) change the compressor inlet and outlet plenums to yield the flow direction of the expander inverse to that of the compressor; (2) change the adapting tube size and valves for the expander use; and (3) change the seal material and lubrication oil for the expander use.

The condenser is a plate heat exchanger with a total heat transfer area of 6.08 m^2. Various instruments are arranged around the ORC loop. The R123 mass flow rate (m_r) is measured by a mass flow meter (MFM). Several measurement points are set around the ORC loop. For instance, points 1, 2, 2′, 3, 4 and 5 refer to expander inlet,

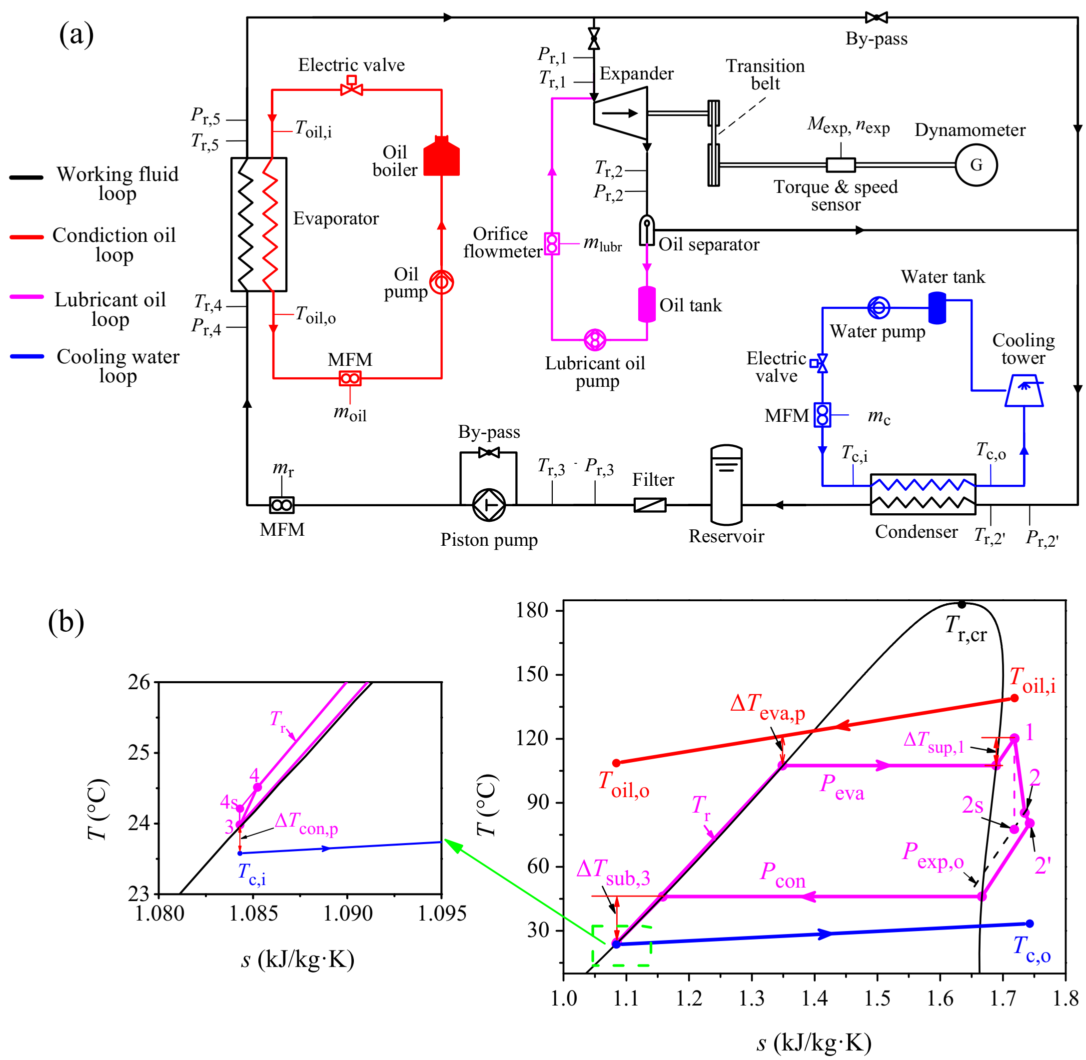

Fig. 2. The ORC system (a) and its cycle (b).

expander outlet, condenser inlet, pump inlet, pump outlet, and evaporator outlet. Correspondingly, pressures and temperatures are marked as $P_{r,1}$, $T_{r,1}$, $P_{r,2}$, $T_{r,2}$, $P_{r,2'}$, $T_{r,2'}$, $P_{r,3}$, $T_{r,3}$, $P_{r,4}$, $T_{r,4}$, $P_{r,5}$, $T_{r,5}$, respectively.

An AC (alternative current) dynamometer dynamically measures the rotating speed (n_{exp}), shaft torque (M_{exp}) and mechanical work ($W_{exp,me}$) of the expander. A frequency converter, an AC motor, a rotating speed sensor, a monitor, a software and transmission facilities are included in the unit. A belt and couplings transmits the power to the AC motor. The transmission ratio is two, yielding the two times of the rotating speed of the expander to that of the AC motor. The rated rotating speed and maximum shaft torque of the AC motor are 1495 rpm and 70.0 N m, respectively.

The computer software dynamically processes the rotating speed and shaft torque of the expander with sensors. The software communicates with the frequency converter to control the shaft torque of the AC motor. During the system operation, the software sets the shaft torque of the AC motor at a specific percentage of the maximum value (70.0 N m here). The frequency converter of the AC motor controls the shaft torque to maintain the desired value. In such a way, the mechanical work of the expander is directly measured, which is

$$W_{exp,me} = \frac{2\pi}{60} M_{exp} n_{exp} \tag{9}$$

3.1.2. The conductive oil loop (red color)

The conductive oil couples the heat source with the ORC cycle. The oil is heated by an electric heater with a 100 kW capacity. The electric heater automatically adjusts the heating power to satisfy the required oil temperature, which can be up to 300 °C, maximally. The present study uses the oil temperatures of 140 °C, 150 °C and 160 °C to evaporate the R123 fluid. The temperature can be controlled with an uncertainty of 1 °C. An oil pump circulates the conductive oil which receives heat from the electric heater and dissipates heat to the ORC evaporator. The oil mass flow rate (m_{oil}) is measured by a mass-flow-meter (MFM). $T_{oil,i}$ and $T_{oil,o}$ are the oil temperature entering and leaving the ORC evaporator. Table 1 shows the major physical properties of the conductive oil. The total heat driving the ORC system is

$$Q_t = m_{oil} C_{P,oil} (T_{oil,i} - T_{oil,o}) \tag{10}$$

Table 1
The physics parameters of the YD-320 conductive oil.

T (°C)	ρ (kg/m^3)	υ (m^2/s)	C_p (kJ/(kg K))	λ (W/(m K))
20	855	2.93×10^{-5}	1.88406	0.49823
50	848	2.21×10^{-5}	1.90918	0.48986
100	821	5.98×10^{-6}	2.1562	0.47311
150	808	2.50×10^{-6}	2.33623	0.45636
200	780	1.16×10^{-6}	2.49952	0.45217
250	757	5.40×10^{-7}	2.67537	0.43124
300	732	3.80×10^{-7}	2.83446	0.41868

3.1.3. The cooling water loop (blue color)

The cooling water loop dissipates extra heat of the ORC system to air environment. The outdoor spray cooling tower is the key component of the cooling water loop. The tower has the cooling capacity of about 73 kW, corresponding to the water flow rate of 5000 kg/h, at which the temperature difference of the cooling water loop is 12.5 °C. The mass flow rate of the cooling water is recorded as m_c. The temperature of the cooling water entering and leaving the ORC condenser are recorded as $T_{c,i}$ and $T_{c,o}$.

3.1.4. The Lubricant oil loop (pink color)

The expander operation needs lubricant. A gear pump circulates the lubricant. The lubricant is mixed with the R123 vapor at the expander inlet. After the expansion, the lubricant is separated from the R123 vapor by an efficient vapor–oil separator. Then, the lubricant returns to the oil tank. A mass flow meter measured the lubricant oil flow rate, which was about 10 kg/s for most of runs in this study. The flow rate of the lubricant was significantly smaller compared with that of the organic fluid.

3.2. The cycle analysis

Fig. 2b shows the ORC cycle. The black envelop is the *T–s* curve of R123, in which $T_{r,cr}$ is the R123 critical temperature. The pink color represents the ORC *T–s* cycle. The red and blue colors represent the variations of the conductive oil and the cooling water. The R123 fluid enters the evaporator at point 4 and leaves the evaporator at point 5. The point 5 is identical to the point 1 by neglecting the pressure drop and heat transfer in the pipeline from the evaporator to the expander. The R123 fluid undergoes the preheating, evaporating and superheating subsections in the evaporator. The heat received by the R123 fluid is

$$Q_t = m_r(h_5 - h_4) = m_r(h_1 - h_4) \tag{11}$$

where h is the specific enthalpy of R123, h_1, h_4 and h_5 are the enthalpies at points of 1, 4 and 5. For the subcritical pressure ORC, the vapor at the evaporator outlet is superheated. The superheating degree is defined as $\Delta T_{sup,1} = T_1 - T_{sat}(P_1)$, in which $T_{sat}(P_1)$ is the saturation temperature corresponding to pressure P_1.

The R123 vapor expands in the expander from point 1 to point 2. The process 1 to 2s represents the isentropic expansion. The expander isentropic efficiency is

$$\eta_{exp,s} = \frac{h_1 - h_2}{h_1 - h_{2s}} \tag{12}$$

where h_1 is the fluid enthalpy at the expander inlet, h_2 and h_{2s} are the enthalpies at point 2 and 2s (isentropic expansion). The expander mechanical efficiency is

$$\eta_{exp,m} = \frac{W_{exp,me}}{m_r(h_1 - h_2)} \tag{13}$$

where $W_{exp,me}$ is the measured expander mechanical work (see Eq. (9)). The experimentally determined expander efficiency is

Table 2
The parameters of main components.

Components	Parameters
Piston pump	Rated flow rate: 2.5 m^3/h
	Rated speed: 720 r/min
Evaporator	Heat transfer area: 5.3 m^2
Condenser	Heat transfer area: 6.1 m^2
Conductive oil boiler	Heating capacity: 100 kW
	Temperature control uncertainty: 1 °C
Cooling tower	Cooling capacity: 73 kW

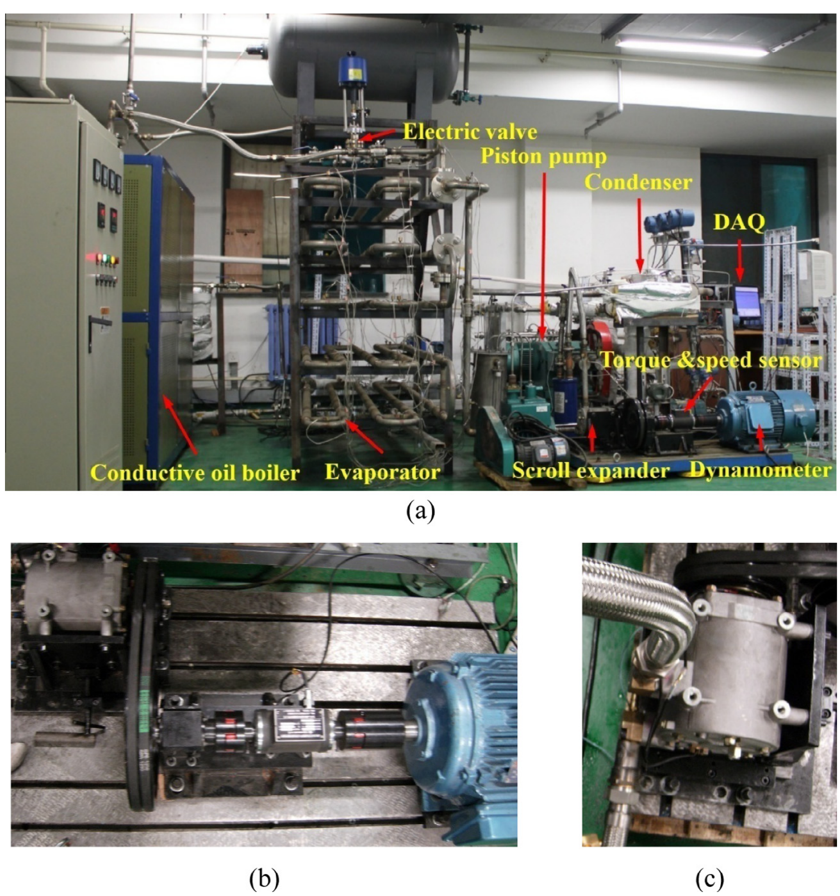

Fig. 3. The ORC Photo (a), the scroll expander and dynamometer (b) and the scroll expander (c).

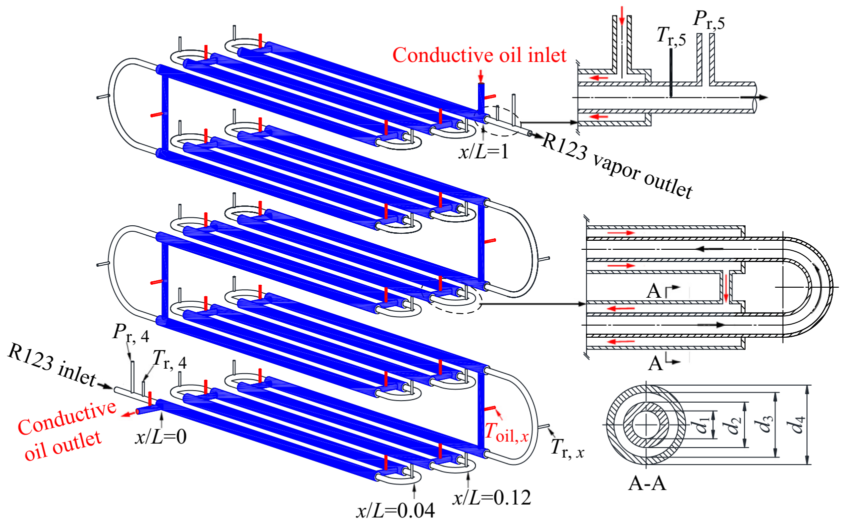

Fig. 4. The concentric tube heat exchanger (evaporator) and the sensor arrangement.

$$\eta_{exp,me} = \eta_{exp,s}\eta_{exp,m} = \frac{W_{exp,me}}{m_r(h_1 - h_{2s})} \tag{14}$$

The R123 fluid is superheated at the expander outlet. The condensation in the condenser is expressed by the process 2′–3. The R123 fluid undergoes single phase vapor cooling, saturation condensation and single phase liquid cooling, consecutively. The subcooling degree at the condenser outlet is $\Delta T_{sub,3} = T_{sat}(P_3) - T_3$. Pumping also causes the entropy increases, represented by process 3–4. The ideal isentropic pumping is represented by the process 3–4s (see the enlarged figure in Fig. 2b). The pumping work is measured by the frequency converter and recorded as $W_{p,me}$. The net work of the ORC system is

$$W_{net,me} = W_{exp,me} - W_{p,me} \tag{15}$$

The net system thermal efficiency is

$$\eta_{net,me} = \frac{W_{net,me}}{Q_t} \tag{16}$$

We performed the exergy analysis of the components and system. Such analysis is widely used for thermal systems [42,43]. The reference state is set as $T_0 = 293.15$ K and $P_0 = 101.3$ kPa. For the organic fluid, the exergy at any state point is

$$E = m_r[(h - h_0) - (s - s_0)] \tag{17}$$

where E is the exergy, m_r is the mass flow rate of the organic fluid, h and s are the enthalpy and entropy at specific state. The subscript 0 refers to the reference state. Thus, the exergy destruction for specific component is

$$I = \sum E_i - \sum E_o \tag{18}$$

The subscripts i and o represent the inlet and outlet. The exergy destruction of the evaporator is

$$I_e = (E_{oil,i} + E_4) - (E_{oil,o} + E_5) \tag{19}$$

where $E_{oil,i}$ and $E_{oil,o}$ are the inlet exergy and outlet exergy of the conductive oil. E_4 and E_5 are the inlet exergy and outlet exergy of the R123 fluid. The system exergy efficiency is

$$\eta_{ex} = \frac{W_{net,me}}{E_{oil,i} - E_{oil,o}} \tag{20}$$

Table 3
Geometric parameters of the evaporator (concentric tube heat exchanger).

Parameter	d_1 (mm)	d_2 (mm)	d_3 (mm)	d_4 (mm)
Level 1, 2 and 3	28	32	48	51
Level 4 and 5	36	42	51	57

Note: locations of d_1, d_2, d_3, d_4 in the A–A cross section can be seen in Fig. 4.

3.3. The ORC machine and evaporator

Fig. 3 shows the developed ORC system. The major components such as conductive oil boiler, evaporator, piston pump, condenser, expander, power generator and data acquisition system are marked. Table 2 shows the major parameters of such components. High accuracy instruments and sensors are used in this study. Pressures, temperatures and mass flow rates are measured by Rosemount 3051 pressure sensor (0.1% uncertainty), WRNK 191 thermocouples (0.5 °C uncertainty) and DMF-1-5-A mass flow meter (0.2% uncertainty), respectively. The torque and rotating speed are measured by JN-338-100A with the uncertainty of 0.1%. The mechanical work is measured by the NY 6000 transducer with the uncertainty of 1 W.

This study used the concentric tube heat exchanger as the evaporator (see Fig. 4). The evaporator had five levels, each level having five tubes. Each tube has 2 m long. Thus, the total effective heat transfer length is $L = 50$ m. The R123 fluid flows in the inner tube. The conductive oil flows in the tube annulus between the inner tube and the outer tube. Heat transfer takes place according to the counter current flows of the conductive oil and the R123 fluid. In the R123 fluid side, different tubes are connected with the horizontal U bend tube at the same level. The tubes at different levels are connected with the vertical U bend tube (marked by black color in Fig. 4). In the conductive oil side, different tube annuluses are connected with the horizontal branch tube[1] (see blue color in Fig. 4). The inner and outer tubes are made from stainless steel. The inner and outer tubes had sizes of ϕ 32 × 2 mm and ϕ 51 × 1.5 mm for levels 1–3, and ϕ 42 × 3 mm and ϕ 57 × 3 mm for levels 4 and 5, respectively (see Table 3 for geometrical parameters of the evaporator). Fig. 4 shows the inlet and outlet of the conductive oil and the R123 fluid. In order to obtain the temperature distribu-

[1] For interpretation of color in Figs. 2 and 4, the reader is referred to the web version of this article.

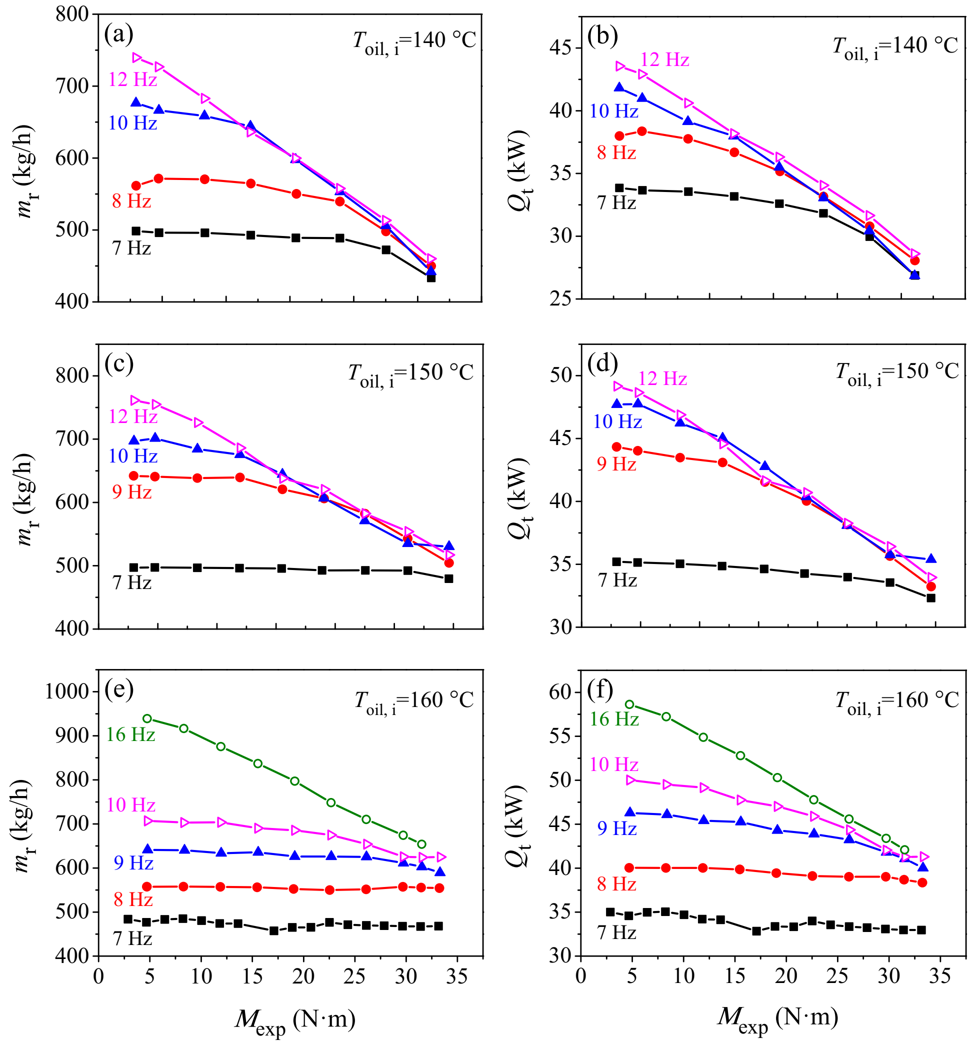

Fig. 5. The mass flow rates of the R123 fluid and the heat received by the evaporator.

tions along the flow direction, a one-dimensional coordinate system was established by stretching the curved U bend tube. The original point ($x = 0$) is located at the R123 fluid inlet, and the ending point is located at the R123 fluid outlet (see bottom-left and top-right corners of Fig. 4). The R123 pressures and temperatures are marked by $P_{r,4}$ and $T_{r,4}$ for the inlet and $P_{r,5}$ and $T_{r,5}$ for the outlet. The evaporator assigns 52 thermocouples to measure the fluid temperatures along the flow direction, half for the conductive oil and half for the R123 fluid. Thermocouples are arranged inside the U bend tube for R123 temperature measurement, and inside the branch tube for the conductive oil temperature measurement. The evaporator outlet and the U bend tube sections are enlarged in Fig. 4.

3.4. The experimental procedure

The ORC performance is influenced by various parameters such as mass flow rates and temperatures of the conductive oil, and mass flow rates, pressures and temperatures of the organic fluid, as well as the cooling water parameters. For given parameters of conductive oil and cooling water, the ORC performance is affected by the pressures and temperatures of the organic fluid. Initially, the ORC system is vacuumed to remove the non-condensable gas. Then, the R123 liquid is charged into the system. Part of the ORC internal volume is occupied by liquid but part of the volume is occupied by the saturated vapor. The present study uses the pumping frequency of the piston pump (f) and the shaft torque of the expander (M_{exp}) as two independent control parameters. Once f and M_{exp} are fixed, all the parameters are stabilized.

Three conductive oil temperatures are 140, 150 and 160 °C, respectively. The oil flow rate is 2150 ± 20 kg/h. The cooling water to condense the R123 vapor has the flow rate of $m_c = 1765 \pm 20$ kg/h. The piston pump frequencies are in the range of 7–16 Hz. The expander torques are in the range of 2.95–29.7 N m.

Fig. 5 shows mass flow rates of the R123 fluid and heating power received by the evaporator dependent on the pumping frequencies (f) and expander torques (M_{exp}). The cases for the three conductive oil temperatures are demonstrated. The mass flow rates of the R123 fluid is less affected by the expander torques at low pumping frequencies. Such trend is more obvious at the conductive oil inlet temperature of $T_{oil,i} = 160$ °C (see Fig. 5e). At high pumping frequencies such as $f > 10$ Hz, m_r is reduced when the expander torques are increased. It is noted that the expander torques quantify the external load of the ORC machine. The right column of Fig. 5 demonstrates the effect of f and M_{exp} on the heating power of the evaporator. The change trend is similar to those of the mass flow rates of the organic fluid. Because the mass flow rates of the R123 fluid are decreased with increases in the expander torques, the heat received by the evaporator from the conductive oil is decreased. In summary, the pumping frequency and the expander torques can be two simple but effective control parameters for ORC applications.

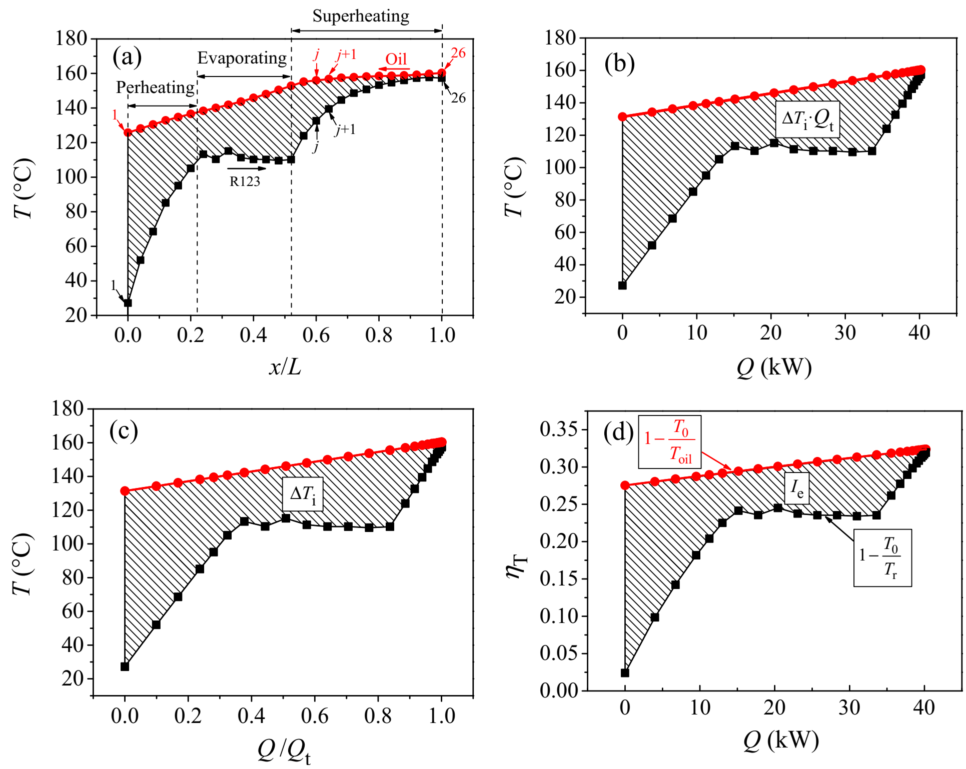

Fig. 6. The integration temperature difference and exergy destruction of the evaporator, based on the measured temperature distribution along the flow length ($T_{oil,i}$ = 160 °C, f = 7 Hz, M_{exp} = 4.75 N m and T_0 = 20 °C).

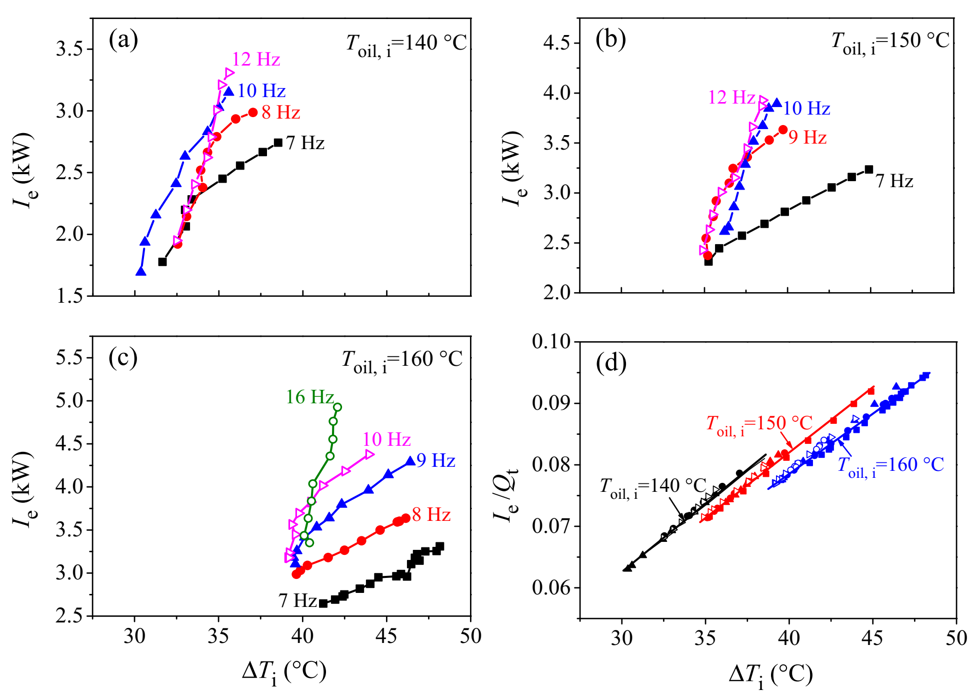

Fig. 7. The exergy destruction (I_e) and the specific exergy destruction (I_e/Q_t) versus the integration temperature difference (ΔT_i) in the evaporator.

4. Results and discussion

4.1. The experimentally determined non-dimensional integration temperature difference

Fig. 6 shows how the integration temperature difference of the evaporator is determined based on the temperature measurements along the evaporator flow length. A case with $T_{oil,i}$ = 160 °C, m_r = 477 kg/h (f = 7 Hz), M_{exp} = 4.75 N m (n_{exp} = 1243 rpm) and W_{exp} = 607 W was shown. Fig. 6a shows T curves for the conductive oil and R123 fluid along the flow length (x/L). The preheating, evaporating and superheating sections are included. The pinch temperature is 3.04 °C and appears at the outlet of x/L = 1.0. We define a pair of thermocouples in the U bend tube for R123 as $T_{r,j}$ and in the vertical connection tube for the conductive oil as $T_{oil,j}$, where the subscript j is the j-th stretched axial location. The next pair of thermocouples will be $T_{r,j+1}$ and $T_{oil,j+1}$. The heat transfer rates between the j-th and $(j+1)$-th stretched axial locations have the following relationship:

$$Q_{j+1} = Q_j + m_{oil}C_{p,oil}(T_{oil,j+1} - T_{oil,j}) \tag{21}$$

In T–Q curves, the coordinates at $j = 1$ are $Q_{j=1} = 0$, $T_{r,j=1} = T_{r,4}$, $T_{oil,1} = T_{oil,o}$. The location at $j = 2$ used the pair of temperatures for the conductive oil and the R123 fluid. The heat transfer rate $Q_{j=2}$ is obtained by Eq. (21). In such a way, the T–Q curves (see Fig. 6b) are reached. Q is non-dimensionalized as Q/Q_t to form the T–(Q/Q_t) curves to have the enclosed area of ΔT_i (see Fig. 6c). For this case, the heat transfer rates for the preheating, evaporation and superheating sections are 12.4 kW, 16.8 kW and 5.4 kW, accounting for 35.87%, 48.49% and 15.64% to the total heat transfer rate, respectively. Fig. 6c shows that the preheating, evaporating and superheating sections cover 53.4%, 39.0% and 7.6% of the integration temperature difference, respectively. The preheating section covers the largest contribution due to the larger local temperature difference between the two fluids and 35.87% of the total heat transfer rate. The superheating section contributes the smallest percentage of the integration temperature difference. Fig. 6d shows that the preheating, evaporating and superheating sections contribute 56.1%, 36.3% and 7.6% of the exergy destructions in the evaporator. Such percentages in Fig. 6d are very close to the integration temperature difference contributions in the three subsections.

Now we examine the relationship between the exergy destruction and the integration temperature difference. Xu et al. [20] noted the linear relationship between them. Fig. 7a–c shows the increased exergy destructions of the evaporator (I_e) with increases in the integration temperature difference (ΔT_i), experimentally. But they do not show the exactly linear relationship. The reason is that the analysis by Xu et al. [20] was performed under the identical heat transfer rates in the evaporator. Alternatively, the data points shown in Fig. 7a–c were performed at a set of fixed pumping frequencies. The ORC operation at a specific pumping frequency does not ensure the same mass flow rates of the R123 fluid and the same heat transfer rate (Q_t) for different data points. Thus, the specific exergy destruction is presented in Fig. 7d, which is expressed as the exergy destruction divided by the heat transfer rate (I_e/Q_t). Physically, the specific exergy destruction (I_e/Q_t) is identical to the entropy generation number (N_s, see Eq. (6)). The perfect linear relationship between I_e/Q_t and ΔT_i is observed, as long as the heat source temperatures $T_{oil,i}$ are the same. Different heat source temperatures yield different linear curves of I_e/Q_t versus ΔT_i (see Fig. 7d).

We plot the specific exergy destructions (I_e/Q_t) versus the first non-dimensional integration temperature difference $\Delta T^*_{i,h} = \Delta T_i/T_{oil,i}$ in Fig. 8a, noting that the temperature unit is K. The perfect linear relationship is found between I_e/Q_t and $\Delta T^*_{i,h}$. The three heat source temperatures of $T_{oil,i}$ = 140, 150 and 160 °C shrink to a single curve. The non-dimensional parameters of I_e/Q_t and $\Delta T^*_{i,h}$ quantify the irreversible exergy loss during the heat transfer process. Fig. 8b plots the specific exergy destructions versus the second non-dimensional integration temperature difference ($\Delta T^*_{i,s} = \Delta T_i/(T_{oil,i} - T_0)$. For each heat source temperature, linear relationship is observed. But the three heat source temperatures $T_{oil,i}$ cannot shrink to a single line. The finding indicates that the first non-dimensional integration temperature difference is better than the second non-dimensional integration temperature difference to quantify the heat exchanger performance. The next section shows that the second one is useful to quantify the evaporator effect on ORCs.

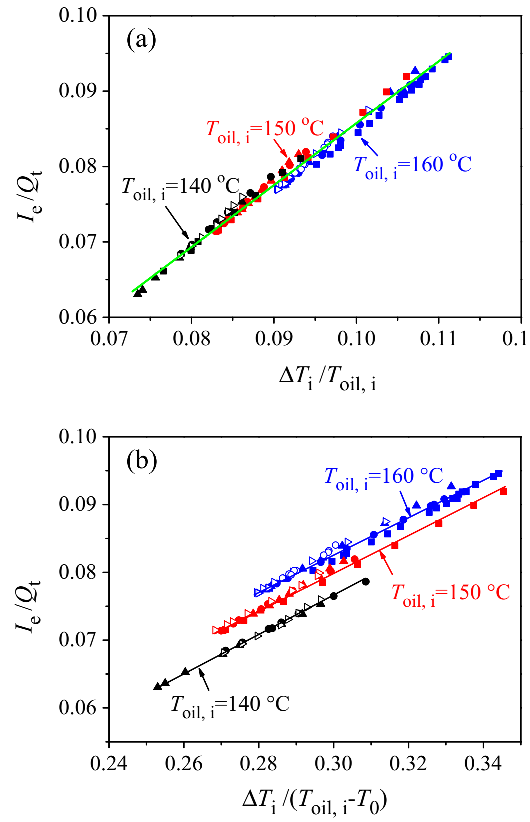

Fig. 8. The specific exergy destruction (I_e/Q_t) versus the first and second non-dimensional integration temperature difference of the evaporator.

4.2. Effect of the second non-dimensional integration temperature difference on ORC

Figs. 9–11 are combined to demonstrate the effects of ΔT_i and $\Delta T^*_{i,s}$ of the evaporator on the ORC performance. The expander mechanical work ($W_{exp,me}$), system thermal efficiency ($\eta_{net,me}$) and exergy efficiency (η_{ex}) are presented. All these parameters are the experimentally determined values.

It is observed that $W_{exp,me}$, $\eta_{net,me}$ and η_{ex} display parabola ($T_{oil,i}$ = 140 °C and 150 °C) or decreased ($T_{oil,i}$ = 160 °C) distributions versus ΔT_i and $\Delta T^*_{i,s}$. At a specific heat source temperature $T_{oil,i}$, the three parameters reached maximum at the same ΔT_i and $\Delta T^*_{i,s}$. The integration temperature difference ΔT_i at which the three parameters reach maximum is 33.8 °C for $T_{oil,i}$ = 140 °C, 36.3 °C for $T_{oil,i}$ = 150 °C and 39.8 °C for $T_{oil,i}$ = 160 °C, respectively. The increase of heat source temperatures slightly increases the integration temperature difference at which the expander mechanical work, system thermal and exergy efficiencies reached maximum. The second non-dimensional integration temperature difference ($\Delta T^*_{i,s}$) equals to 0.282 at which the system performance parameters reached maximum. No matter for what mass flow rates of the organic fluid, heating powers received from the heat source, expander rotating speeds and torques and the heat source temperatures, the ORC system can reach the optimal performance at a specific second non-dimensional integration temperature difference. The second non-dimensional integration temperature difference quantifies the coupling between the heat source and the ORC system and it is also capable of considering the temperature difference within the heat source and the environment for thermal-power conversion system. It can be regarded as an important parameter index for ORC system optimization. It is noted that the value of 0.282 is determined by the experiment. The value

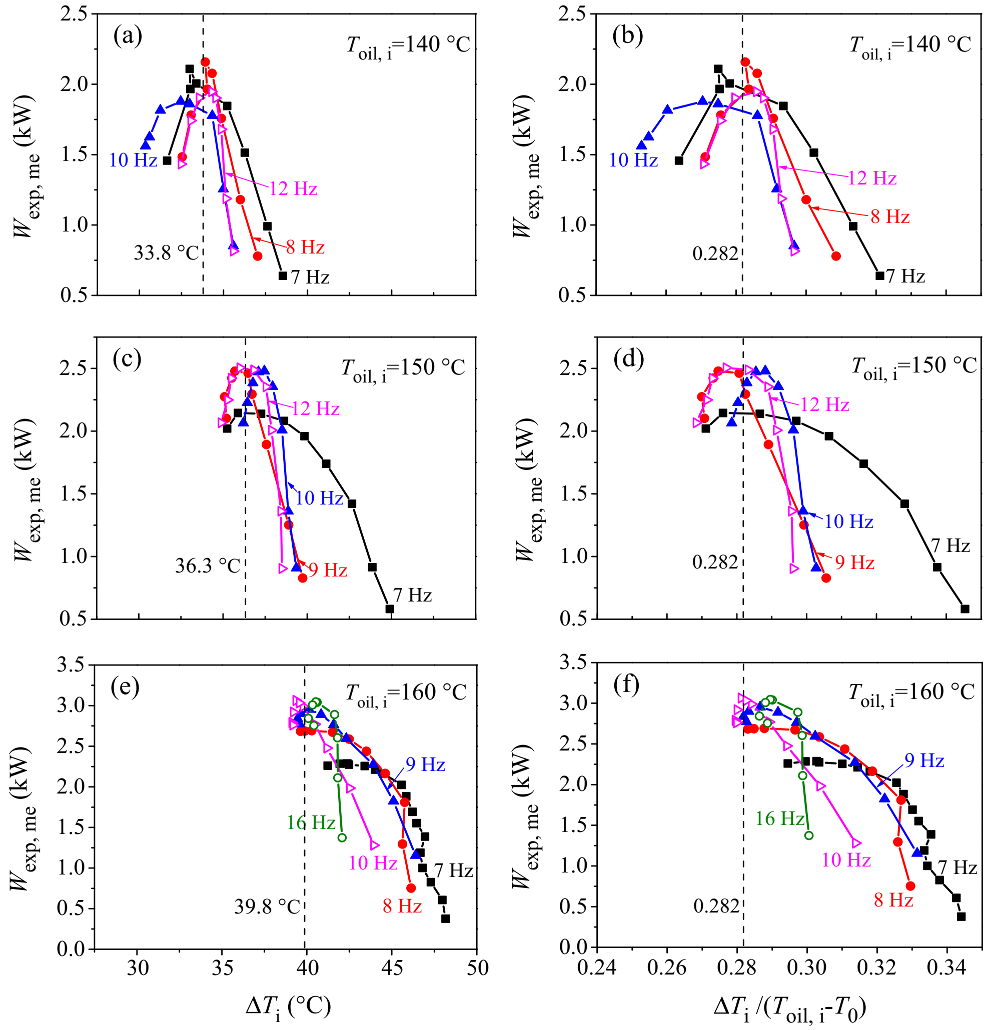

Fig. 9. The mechanical work of the expander versus the integration temperature difference and the second non-dimensional integration temperature difference of the evaporator.

may be changed for different ORC design. The general consideration of the second non-dimensional integration temperature difference on ORCs should be further investigated.

4.3. Explanation of the observed phenomenon

Section 4.2 described the parabola or decreased ORC performance parameters versus integration temperature differences. All the three performance parameters show similar distributions, reaching maximum at $\Delta T^*_{i,s} = 0.282$. In Fig. 11b, three points of *a*, *b* and *c* are marked with $f = 8$ Hz and $T_{oil,i} = 140$ °C, locating at $\Delta T^*_{i,s} = 0.271$, 0.283 and 0.300, respectively. The following analysis was focused on the curve with $f = 8$ Hz for $T_{oil,i} = 140$ °C. The point *b* represents the maximum condition. The performances are divided into two regimes: regime 1 before the maximum point *b* and regime 2 beyond the maximum point *b*.

Fig. 12a shows how $\Delta T^*_{i,s}$ influences $\eta_{exp,me}$ (expander efficiencies) and $\Delta T_{sup,1}$ (vapor superheating at expander inlet). The two regimes are marked by the yellow and white colors respectively, interfaced at the maximum point. In regime 1, $\eta_{exp,me}$ are small but increased and $\Delta T_{sup,1}$ is about zero to show the saturated vapor state, with increases in $\Delta T^*_{i,s}$, until the maximum $\eta_{exp,me}$ is reached to 0.606 at point *b*. We note that $\eta_{exp,me}$ is the isentropic efficiency $\eta_{exp,s}$ multiplied by the mechanical efficiency $\eta_{exp,m}$ (see Eqs. (12)–(14)). Fig. 12b shows $\eta_{exp,m}$ and $\eta_{exp,s}$ versus $\Delta T^*_{i,s}$, in which $\eta_{exp,m}$ shows the similar distribution as that of $\eta_{exp,me}$, but $\eta_{exp,s}$ are smaller in regime 1 than those in regime 2. The increase of $\Delta T^*_{i,s}$ decreases the pressure ratios of P_1/P_2 and temperature difference across the expander ΔT_{exp}.

The expander efficiencies are decreased from $\eta_{exp,me} = 0.606$ at point *b* to 0.427 at point *a* in regime 1 (see Fig. 12a), causing the significantly decreased expander mechanical work and system thermal and exergy efficiencies (see Figs. 9–11). From point *b* to point *a*, the integration temperature differences are decreased and the saturated vapor exists at the expander inlet. This finding does not support the thermodynamic analysis. The ORC theoretical analysis yields the maximum work output and higher thermal efficiencies with saturated vapor at the expander inlet [24]. Alternatively, our theoretical analysis indicates the improved thermal performance when the integration temperature differences are decreased to decrease the exergy loss of the evaporator [19,20].

The deviation of the present study from the theoretical work lies in the vapor cavitation phenomenon, which is neglected in the theoretical analysis. We explain the vapor cavitation based on the non-equilibrium evaporation heat transfer in the evapora-

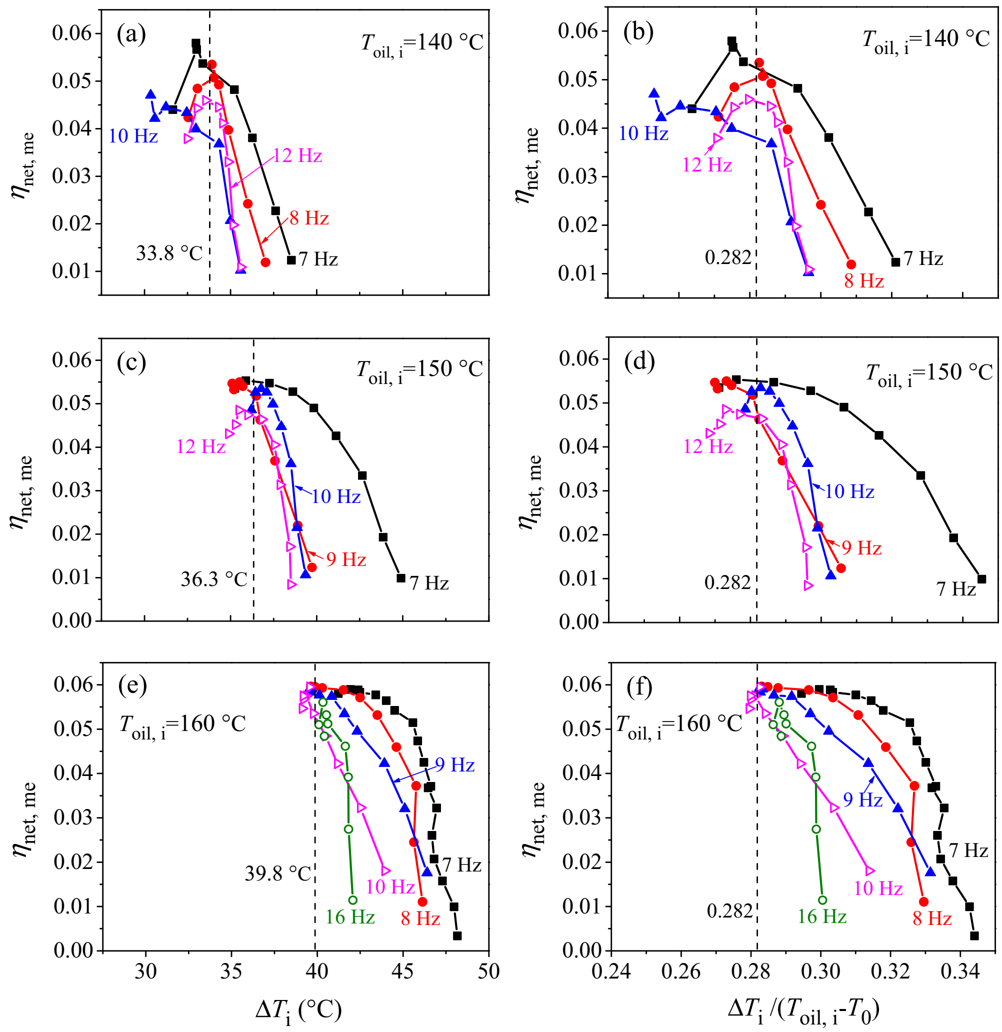

Fig. 10. The ORC net thermal efficiencies versus the integration temperature difference and the second non-dimensional integration temperature difference of the evaporator.

tor. During the convective evaporation heat transfer in the tube, liquid films exist on the tube wall. Shear-stress on the vapor–liquid interface entrains liquid droplets in the vapor. The temperature difference between vapor and liquid droplets is called the thermal non-equilibrium. The saturated vapor, based on the equilibrium thermodynamics, contains liquid droplets. When liquid droplets enter the expander, they attack the expander blade. The shock wave is created in a very short period of time (10^{-8} s scale [44]) during the droplet attacking process. A strong mechanical force is formed for such attacking. The droplet induced shock wave and mechanical force disturb the flow field in the expander. Thus, the expander mechanical work is decreased. The shock wave phenomenon also shortens the expander lifetime. The successful way to avoid the shock wave in the expander is to increase the vapor superheating at the expander inlet, under which liquid droplets do not exist. The increase of the vapor superheating causes the raise of the integration temperature difference. Fewer studies investigated the effect of the vapor superheatings on the expander performance. Gao et al. [45] used the scroll expander with R245fa as the working fluid. They found the maximum expander mechanical work at the vapor superheating of about 28 °C. Lee et al. [46] used the screw expander and plate heat exchangers. The system was unstable and thermal efficiency was low for vapor superheatings lower than 10 °C.

The ORC performance in regime 2 supports our previous study regarding the integration temperature difference [20]. From point *b* to *c*, the increment of the integration temperature difference raises the exergy destruction of evaporator and vapor superheatings at the expander inlet. Thus, the expander mechanical work and system thermal and exergy efficiencies are decreased.

Fig. 13 shows the *T–s* curves at the three points of *a*, *b* and *c*. At point *a* (see Fig. 13a), the thermal match between the heat source and the R123 fluid is the best. But the saturated vapor at the expander inlet causes the vapor cavitation in the expander to lower the expander performance. Thus, the system thermal and exergy efficiencies are 4.2% and 15.7% respectively. At point *b* (see Fig. 13b), the vapor superheating degree is 12.7 °C. The point *b* is the critical condition under which the vapor cavitation in the expander begins to disappear. The integration temperature difference of the evaporator is acceptable (but not the smallest). Thus, the system thermal and exergy efficiencies are 5.4% and 20.2%, respectively. These efficiencies are the largest at the heat source temperature of 140 °C. At point *c* (see Fig. 13c), the system performance returns to be worse. The apparently large second non-dimensional integration temperature difference causes large vapor superheating degrees at the expander inlet to worsen the thermal match between the conductive oil and the R123 fluid. Besides, the large integration temperature difference of the evaporator also

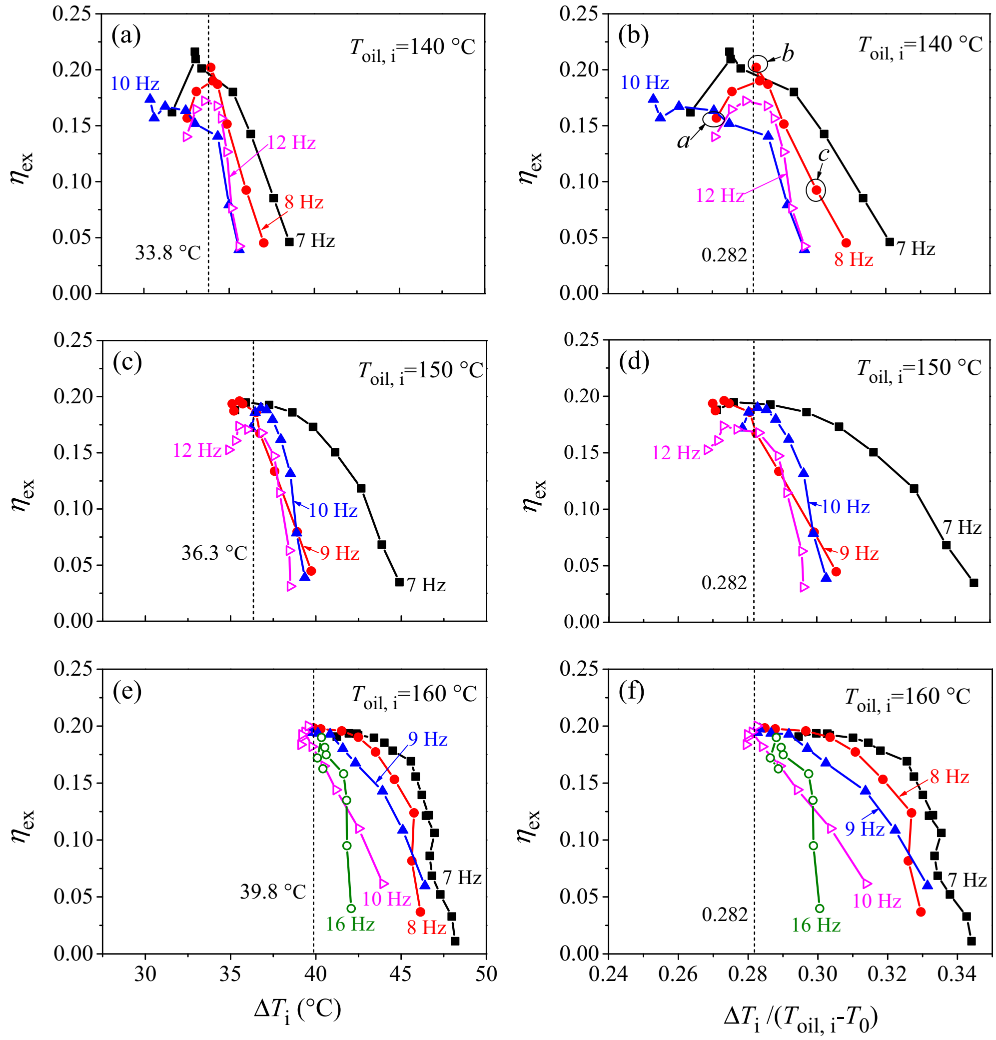

Fig. 11. The ORC system exergy efficiencies versus the integration temperature difference and the second non-dimensional integration temperature difference of the evaporator.

yields the large vapor superheating degree at the condenser inlet to worsen the thermal match between the R123 fluid and the cooling water.

Fig. 14 shows the effect of the integration temperature differences on the exergy loss distributions. The system available exergy E_a is the exergy difference for the conductive oil entering and leaving ORC: $E_a = E_{oil,i} - E_{oil,o}$. Part of E_a is converted into expander mechanical work, $W_{exp,me}$. The left is consumed by exergy destructions in the pump, evaporator, expander and condenser. The following relationship exists:

$$E_a = W_{exp,\,me} + \sum I \tag{22}$$

The contribution of each item in the right side of Eq. (22) identifies the useful exergy and non-useful exergy distributions. In Fig. 14, I_{other} refers to the exergy destruction due to the heat loss and pressure drops in pipelines, which is small. With continuous increases of the second non-dimensional integration temperature differences, the evaporator and condenser increased the exergy destruction contributions, from point *a* to *c*. Regarding the evaporator, the I_e/E_a values are 24.4%, 26.2% and 28.4%, respectively; regarding the condenser, the I_{con}/E_a values are 27.1%, 31.9% and 40.8%, respectively. The increase of the integration temperature difference of the evaporator elongates the superheating section to raise the exergy destruction of the condenser. Special attention is paid to the expander. The expander mechanical work is small and the exergy destruction by the expander is large, due to the saturated vapor expansion at point *a*. The point *b* had largest expander mechanical work and smallest exergy destruction at which the vapor cavitation begins to disappear. The point *c* returns to lower the expander mechanical work and increase the exergy destruction, due to the increased integration temperature difference of the evaporator.

4.4. Comments, applications and future work

4.4.1. The original contribution of this paper

Temperature difference is a widely used term. The temperature differences such as the logarithmic-mean-temperature-difference and the pinch temperature difference, are defined at specific locations. They are helpful for the heat transfer estimation but have no connection with the exergy loss of the heat exchanger. The major contribution of this paper is to define two non-dimensional integration temperature differences. The first non-dimensional integration temperature difference is linear to the specific exergy destruction, or the entropy generation number. It connects the exergy destruction and the heat transfer process. It is useful to evaluate the heat exchanger performance, from the thermodynamic and heat transfer points of view.

The second non-dimensional integration temperature difference reflects the evaporator effect on the ORC system. It compre-

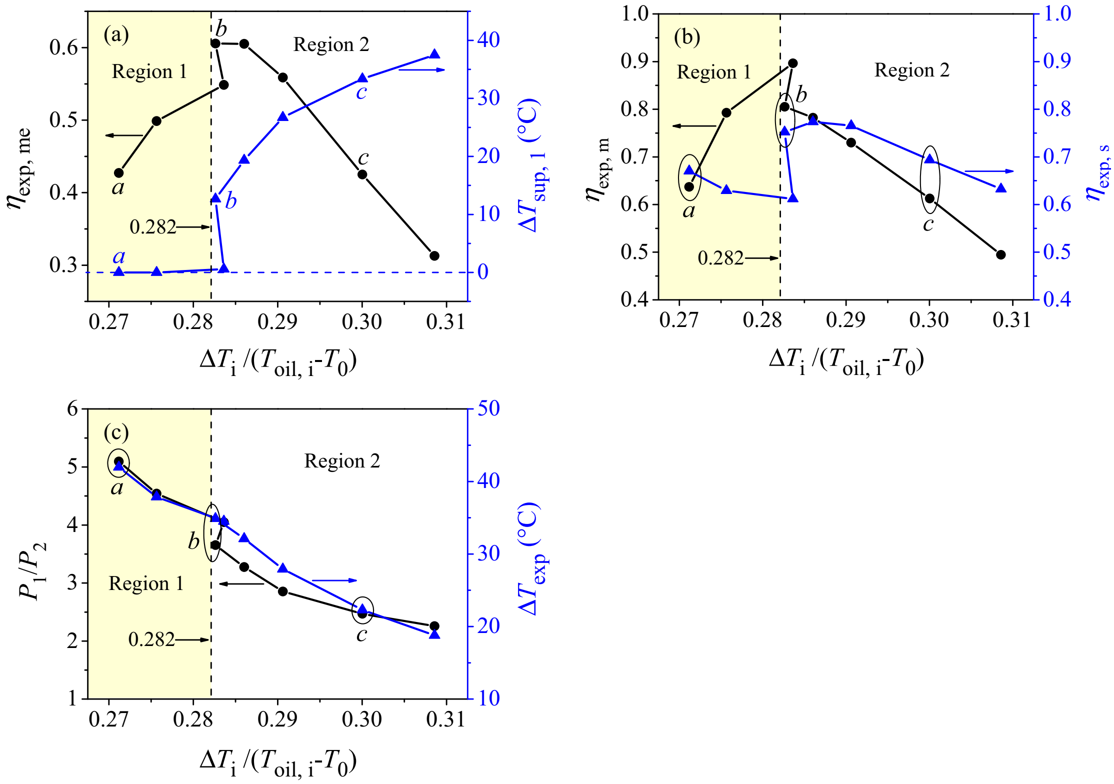

Fig. 12. The expander efficiencies and pressure ratios versus the second non-dimensional integration temperature difference ($T_{oil,i}$ = 140 °C, f = 8 Hz).

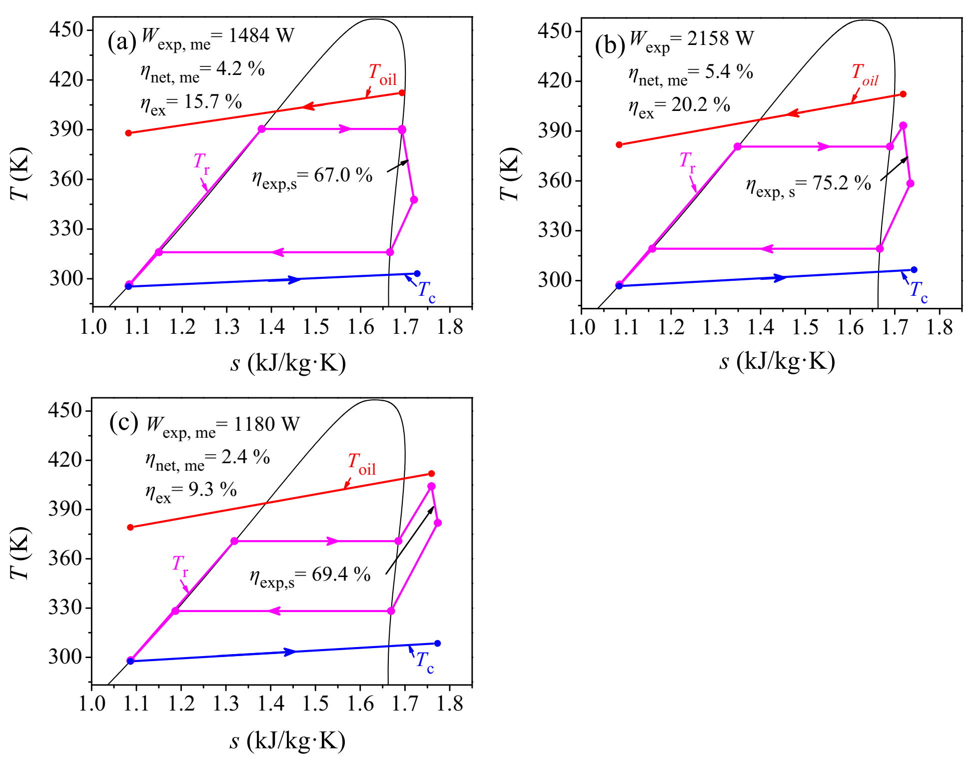

Fig. 13. The T–s cycles at the three points of a, b and c with $T_{oil,i}$ = 140 °C and f = 8 Hz.

hensively considers various factors such as the heat source temperature, heating powers received from the heat source, mass flow rates of the organic fluid and expander torques. Physically, it reflects the coupling between heat source and thermal engine referenced to the environment temperature. It adjusts the exergy destructions of various components to optimize the system performance. It can be an important non-dimensional parameter for the system optimization.

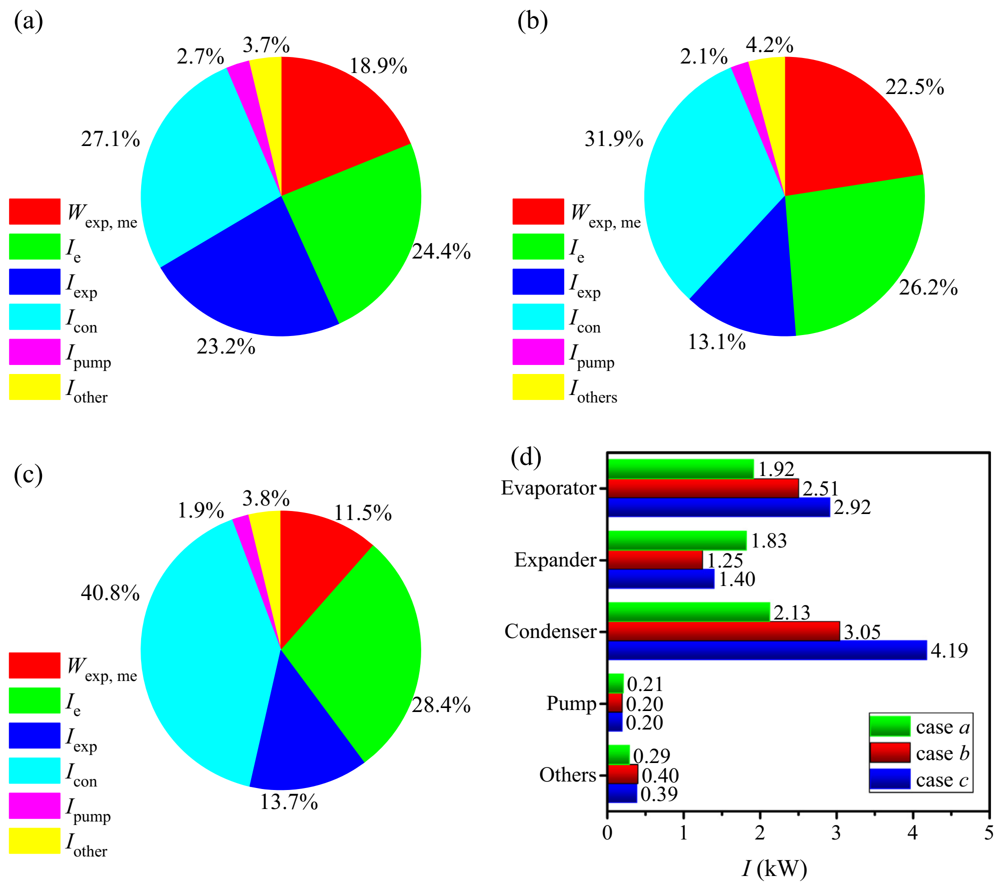

Fig. 14. The useful exergy (expander mechanical work) and exergy destructions in each component of the ORC system at the three points of *a*, *b* and *c*.

The new finding of this paper did not support the conclusion "the smaller the exergy destruction of the evaporator, the better the system performance is". The smallest exergy destruction happens with the saturation vapor outlet of the evaporator. This will cause the vapor cavitation in the expander, which is neglected in available references [33,47,48]. The ORC optimal condition occurs when the vapor cavitation in the expander disappears and the exergy destructions in the evaporator and condenser are acceptable, under which the expander has largest work output.

Finally, it is noted that most of articles [24,25,47] optimized the system considering the thermal efficiencies but neglecting the heat utilization degree. The useful work output is the product of the thermal efficiency multiplying by the recovered heat from the heat source. Thus, the thermal efficiency is high but the useful work can be low. One expects to obtain a maximum work output for a heat source. This paper identified that the thermal efficiency and expander mechanical work can reach maximum values simultaneously at $\Delta T^*_{i,s} = 0.282$. It is noted that the value of 0.282 may be changed for different ORC design.

4.4.2. Applications of the non-dimensional integration temperature difference

The major contribution of this paper is to define two non-dimensional integration temperature differences, linking the heat transfer and the thermodynamics. The non-dimensional integration temperature differences are useful to evaluate either the heat exchanger itself or the system performance of the thermal engine. Especially, the second non-dimensional integration temperature difference balances the exergy losses of various components of the ORC system to optimize the system.

The concept can be used for the optimal ORC design. The application includes two steps. The first step is to obtain the non-dimensional integration temperature difference of the evaporator. The second step is to obtain the performance parameters such as the system thermal and exergy efficiencies as well as the expander work related to the non-dimensional integration temperature difference. The optimal points are achievable after the two steps are over. In order to do so, the objective parameters or some initial conditions should be given. These parameters include the expected system efficiency and the expander work output. The initial condition parameters include the temperature and the flow rate of the heat carrier fluid of the heat source. The present study used the experimental data, but the non-dimensional integration temperature difference and the system performance parameters can be calculated theoretically. The optimal design helps to determine the types and sizes of the components. The organic fluid can also be determined to have a higher thermal performance.

For an established ORC system, the non-dimensional integration temperature difference can be used to optimize the operating parameters, such as the pressure and flow rate of the organic fluid, the enthalpy difference across various components and the pressure ratio across the expander. When the system is operating at these optimal parameters, the system should have the largest thermal efficiency and the work output. In summary, the non-dimensional integration temperature difference can be used for both the ORC design and the operation.

4.4.3. Future work of the non-dimensional integration temperature difference

This is a preliminary study on the first and second non-dimensional integration temperature differences. An optimal second non-dimensional integration temperature difference was 0.282, under which the thermal efficiency and expander work reached maximum, simultaneously. The value of 0.282 may be different for different ORC systems. The present ORC system is a subcritical pressure one, using R123 as the working fluid. The future investigation on the non-dimensional integration temperature difference should be continued regarding the trans-critical pressure ORC and the subcritical pressure ORC with the mixture working fluids. The present study used the conductive oil as the heat source. The different heat sources such as solar thermal energy or geothermal water heat source will be tried to verify the correctness and usefulness of the non-dimensional integration temperature difference.

From the purely thermodynamic point of view, the smaller the integration temperature difference, the better the ORC performance is. This conclusion is limited by the expander performance. Thus, an optimal second non-dimensional integration temperature difference exists to avoid the vapor cavitation in the expander. The future work is also suggested on the integration temperature differences using different types of expanders.

Various ORC optimization models are proposed in the literature [6,27,31]. These references used the purely thermodynamic assumptions such as the saturation vapor at the expander inlet and the saturation liquid at the pump inlet. Under many situations, these assumptions are difficult to be fulfilled for practical applications. This is the reason that the "optimal" ORC performance is difficult to be reached. The optimal second non-dimensional integration temperature difference is obtained by the vapor cavitation limit in the expander. The future work should be continued on the theoretical/numerical study on the integration temperature difference to form a general framework of the optimization model, that is thoroughly different from those reported in the references.

5. Conclusions

Two non-dimensional integration temperature differences are newly defined in this paper. The first one is the integration temperature difference divided by the temperature of the hot fluid entering the heat exchanger. It is useful for the performance evaluation of the heat exchanger itself. The second one is the integration temperature difference divided by the temperature difference between the heat source temperature and the environment temperature. It is helpful to evaluate the effect of the heat exchanger on the thermal to power conversion system.

An experimental setup was developed. Specifically, 26 pairs of thermocouples were arranged along the flow length of the evaporator. The spartial temperature distribution was used to obtain the integration temperature difference of the evaporator. It was shown that the first non-dimensional temperature difference is linear to the specific entropy generation numbers, for different operating parameters of the heat source and the organic fluid.

The expanders, system thermal and exergy efficiencies show parabola distributions versus the second non-dimensional temperature differences. Beyond the optimal points, the system performances are deteriorated either by the vapor cavitation in the expander for regime 1, or by the poor thermal matches of the two fluids in the evaporator and condenser for regime 2. The system performance is best when the second non-dimensional integration temperature difference equals to 0.282. An acceptable (but not the smallest) exergy destruction of the evaporator is useful to avoid the vapor cavitation in the expander. The second non-dimensional temperature difference balances various exergy losses of the ORC system to elevate the expander performance. It guides engineers to reach maximum work output with specific heat source.

The applications and the future work of the non-dimensional integration temperature difference are described in the end of this paper.

Acknowledgement

This paper was financially supported by the Natural Science Foundation of China with the contract numbers of (51210011 and 51436004).

References

[1] Nafey AS, Sharaf MA. Combined solar organic Rankine cycle with reverse osmosis desalination process: energy, exergy, and cost evaluations. Renew Energy 2010;35(11):2571–80.
[2] Al-Sulaiman FA, Dincer I, Hamdullahpur F. Exergy modeling of a new solar driven trigeneration system. Sol Energy 2011;85(9):2228–43.
[3] Ratlamwala TAH, Dincer I, Aydin M. Energy and exergy analyses and optimization study of an integrated solar heliostat field system for hydrogen production. Int J Hydrogen Energy 2012;37(24):18704–12.
[4] Sun ZX, Wang JF, Dai YP, Wang JH. Exergy analysis and optimization of a hydrogen production process by a solar-liquefied natural gas hybrid driven transcritical CO_2 power cycle. Int J Hydrogen Energy 2012;37(24):18731–9.
[5] Ahmadi P, Dincer I, Rosen MA. Energy and exergy analyses of hydrogen production via solar-boosted ocean thermal energy conversion and PEM electrolysis. Int J Hydrogen Energy 2013;38(4):1795–805.
[6] Heberle F, Bruggemann D. Exergy based fluid selection for a geothermal Organic Rankine Cycle for combined heat and power generation. Appl Therm Eng 2010;30(11):1326–32.
[7] El-Emam RS, Dincer I. Exergy and exergoeconomic analyses and optimization of geothermal organic Rankine cycle. Appl Therm Eng 2013;59(1):435–44.
[8] Tunc M, Sisbot S, Camdali U. Exergy analysis of electricity generation for the geothermal resources using organic rankine cycle: kzldere-denizli case. Environ Prog Sustain Energy 2013;32(3):830–6.
[9] Imran M, Usman M, Park BS, Kim HJ, Lee DH. Multi-objective optimization of evaporator of organic Rankine cycle (ORC) for low temperature geothermal heat source. Appl Therm Eng 2015;80:1–9.
[10] Al-Sulaiman FA, Hamdullahpur F, Dincer I. Greenhouse gas emission and exergy assessments of an integrated organic Rankine cycle with a biomass combustor for combined cooling, heating and power production. Appl Therm Eng 2011;31(4):439–46.
[11] Al-Sulaiman FA, Dincer I, Hamdullahpur F. Energy and exergy analyses of a biomass trigeneration system using an organic Rankine cycle. Energy 2012;45(1):975–85.
[12] He MG, Zhang XX, Zeng K, Gao K. A combined thermodynamic cycle used for waste heat recovery of internal combustion engine. Energy 2011;36:6821–9.
[13] Zhou NJ, Wang XY, Chen Z, Wang ZQ. Experimental study on Organic Rankine Cycle for waste heat recovery from low-temperature flue gas. Energy 2013;55:216–25.
[14] Minea V. Power generation with ORC machines using low-grade waste heat or renewable energy. Appl Therm Eng 2014;69:143–54.
[15] Yang MH, Yeh RH. Analyzing the optimization of an organic Rankine cycle system for recovering waste heat from a large marine engine containing a cooling water system. Energy Convers Manage 2014;88:999–1010.
[16] Guillen D, Klockow H, Lehar M, Freund S, Jackson J. Development of a direct evaporator for the organic Rankine cycle. In: Energy technology 2011: carbon dioxide and other greenhouse gas reduction metallurgy and waste heat recovery; 2011. p. 25–35.
[17] Chen QC, Xu JL, Chen HX. A new design method for Organic Rankine Cycles with constraint of inlet and outlet heat carrier fluid temperatures coupling with the heat source. Appl Energy 2012;98:562–73.
[18] Zhang HG, Wang EH, Fan BY. Heat transfer analysis of a finned-tube evaporator for engine exhaust heat recovery. Energy Convers Manage 2013;65:438–47.
[19] Xu JL, Yu C. Critical temperature criterion for selection of working fluids for subcritical pressure Organic Rankine cycles. Energy 2014;74:719–33.
[20] Yu C, Xu JL, Sun YS. Transcritical pressure Organic Rankine Cycle (ORC) analysis based on the integrated-average temperature difference in evaporators. Appl Therm Eng 2014;88:2–13.
[21] Xu JL, Liu C. Effect of the critical temperature of organic fluids on supercritical pressure Organic Rankine Cycles. Energy 2013;63:109–22.
[22] Yang K, Zhang HG, Wang Z, Zhang J, Yang FB, Wang EH, et al. Study of zeotropic mixtures of ORC (organic Rankine cycle) under engine various operating conditions. Energy 2013;58:494–510.
[23] Lecompte S, Ameel B, Ziviani D, van den Broek M, De Paepe M. Exergy analysis of zeotropic mixtures as working fluids in Organic Rankine Cycles. Energy Convers Manage 2014;85:727–39.
[24] Saleh B, Koglbauer G, Wendland M, Fischer J. Working fluids for low-temperature organic Rankine cycles. Energy 2007;32:1210–21.
[25] Liu Q, Duan YY, Yang Z. Effect of condensation temperature glide on the performance of organic Rankine cycles with zeotropic mixture working fluids. Appl Energy 2014;115:394–404.

[26] Yang XF, Xu JL, Miao Z, Zou JH, Yu C. Operation of an organic Rankine cycle dependent on pumping flow rates and expander torques. Energy 2015;90:864–78.
[27] Song J, Gu CW. Performance analysis of a dual-loop organic Rankine cycle (ORC) system with wet steam expansion for engine waste heat recovery. Appl Energy 2015;156:280–9.
[28] Maraver D, Royo J, Lemort V, Quoilin S. Systematic optimization of subcritical and transcritical organic Rankine cycles (ORCs) constrained by technical parameters in multiple applications. Appl Energy 2014;117:11–29.
[29] Toffolo A, Lazzaretto A, Manente G, Paci M. A multi-criteria approach for the optimal selection of working fluid and design parameters in Organic Rankine Cycle systems. Appl Energy 2014;121:219–32.
[30] Lee DS, Hung TC, Lin JR, Zhao J. Experimental investigations on solar chimney for optimal heat collection to be utilized in organic Rankine cycle. Appl Energy 2015;154:651–62.
[31] Sun FM, Ikegami Y, Jia B, Arima H. Optimization design and exergy analysis of organic rankine cycle in ocean thermal energy conversion. Appl Ocean Res 2012;35:38–46.
[32] Wang JF, Dai YP, Gao L. Exergy analyses and parametric optimizations for different cogeneration power plants in cement industry. Appl Energy 2009;86:941–8.
[33] Cavazzini G, Dal Toso P. Techno-economic feasibility study of the integration of a commercial small-scale ORC in a real case study. Energy Convers Manage 2015;99:161–75.
[34] Wang HR, Xu JL, Yang XF, Miao Z, Yu C. Organic Rankine cycle saves energy and reduces gas emissions for cement production. Energy 2015;86:59–73.
[35] Witte LC, Shamsundar N. A thermodynamic efficiency concept for heat exchange devices. J Eng Gas Turbines Power 1983;105(1):199–203.
[36] Manjunath K, Kaushik SC. Second law thermodynamic study of heat exchangers: a review. Renew Sustain Energy Rev 2014;40:348–74.
[37] Baehr HD, Stephan K. Heat and mass transfer. 2nd ed. Berlin: Springer; 2006.
[38] Li YR, Wang JN, Du MT. Influence of coupled pinch point temperature difference and evaporation temperature on performance of organic Rankine cycle. Energy 2012;42:503–9.
[39] Zebian H, Mitsos A. A double-pinch criterion for regenerative Rankine cycles. Energy 2012;40:258–70.
[40] Yu HS, Feng X, Wang YF. A new pinch based method for simultaneous selection of working fluid and operating conditions in an ORC (Organic Rankine Cycle) recovering waste heat. Energy 2015;90:36–46.
[41] Chang JC, Hung TC, He YL, Zhang W. Experimental study on low-temperature organic Rankine cycle utilizing scroll type expander. Appl Energy 2015;155:150–9.
[42] Bao JJ, Zhao L. Exergy analysis and parameter study on a novel auto-cascade Rankine cycle. Energy 2012;48:539–47.
[43] Kaska O. Energy and exergy analysis of an organic Rankine for power generation from waste heat recovery in steel industry. Energy Convers Manage 2014;77:108–17.
[44] Li N, Zhou Q, Chen X, Xu T, Hui S, Zhang D. Liquid drop impact on solid surface with application to water drop erosion on turbine blades, part I: nonlinear wave model and solution of one-dimensional impact. Int J Mech Sci 2008;50(10):1526–42.
[45] Gao P, Jiang L, Wang LW, Wang RZ, Song FP. Simulation and experiments on an ORC system with different scroll expanders based on energy and exergy analysis. Appl Therm Eng 2015;75:880–8.
[46] Lee YR, Kuo CR, Liu CH, Fu BR, Hsieh JC, Wang CC. Dynamic response of a 50 kW organic Rankine cycle system in association with evaporators. Energies 2014;7:2436–48.
[47] Mago PJ, Srinivasan KK, Chamra LM, Somayaji C. An examination of exergy destruction in organic Rankine cycles. Int J Energy Res 2008;32(10):926–38.
[48] Mago PJ, Chamra LM. Exergy analysis of a combined engine-organic Rankine cycle configuration. Proc Inst Mech Eng Part A J Power Energy 2008;222:761–70.